Simulations of Solar Granulation: I. General Properties

R. F. Stein

Dept. of Physics and Astronomy, Michigan State University, East Lansing, MI 48823, U.S.A.

and

Å. Nordlund

Theoretical Astrophysics Center and Astronomical Observatory / NBIfAFG,
Juliane Maries Vej 30, Dk-2100 Copenhagen Ø, Denmark

ABSTRACT

Numerical simulations provide information on solar convection not available by direct observation. We present results of simulations of near surface solar convection with realistic physics – an equation of state including ionization and three-dimensional, LTE radiative transfer using a four bin opacity distribution function. Solar convection is driven by radiative cooling in the surface thermal boundary layer, producing the familiar granulation pattern. In the interior of granules, warm plasma ascends with $\approx 10\%$ ionized hydrogen. As it approaches and passes through the optical surface, the plasma cools, recombines and loses entropy. It then turns over and converges into the dark intergranular lanes and further into the vertices between granulation cells. These vertices feed turbulent downdrafts below the solar surface, which are the sites of buoyancy work that drives the convection. Only a tiny fraction of the fluid ascending at depth reaches the surface to cool, lose entropy and form the cores of these downdrafts. Granules evolve by pushing out against and being pushed in by their neighboring granules, and by being split by overlying fluid that cools and is pulled down by gravity. Convective energy transport properties that are closely related to integral constraints such as conservation of energy and mass, are exceedingly robust. Other properties, that are less tightly constrained, and / or involve higher order moments or derivatives are found to depend more sensitively on the numerical resolution. At the highest numerical resolution, excellent agreement between simulated convection properties and observations is found. In interpreting observations it is crucial to remember that surfaces of constant optical depth are corrugated. The surface of unit optical depth in the continuum is higher above granules and lower in the intergranular lanes, while the surface of optical depth unity in a spectral line is corrugated in ways that are influenced by both thermal and Doppler effects.

Subject headings: sun:convection- sun:granulation- sun:numerical simulation- computational fluid dynamics

1. Introduction

In the outer third of the Sun energy is transported primarily by convection, rather than by photons. Convection, however, does much more than merely transport energy to the solar surface. Convective motions together with rotation are believed to drive the dynamo that reverses the surface magnetic field with an 11 year time scale. Convective motions generate the p-mode oscillations that are used to probe the solar interior. They also produce magneto-hydrodynamic waves that supply energy to the solar chromosphere, and they move the footpoints of the coronal magnetic flux tubes, which leads to magnetic reconnection that heats the corona. Convective motions provide support for the solar atmosphere in addition to that provided by the plasma pressure, thereby extending the resonant cavities of the p-modes and altering their frequencies from those calculated for a static solar model. Convective motions transport angular momentum and thoroughly mix the material in the outer third of the sun, while downdrafts penetrating into the stable sub-convective region mix material to some extent there as well.

Recent, high resolution ground based observations (Title et al. 1992; Wang et al. 1995; Berger & Title 1996) and "seeing" free satellite observations (Title et al. 1989; Schrijver et al. 1997) have provided a wealth of new information about solar convection. SOHO and GONG oscillation data are, for the first time, revealing information about the subsurface nature of convection (Kosovichev 1996; Duvall et al. 1997). Hence, this is an opportune time to make comparisons between theoretical convection models and observational results.

Convection is a difficult process to understand because it is chaotic, non-local, three-dimensional, and involves non-linear interactions over many disparate length scales. Several complementary approaches are being used to study it. Laboratory experiments (Zocchi et al. 1990) have demonstrated the crucial role of boundary layers in determining the nature of the convection and the amount of energy transported. Numerical simulations using simple, ideal physics have: revealed the asymmetry between up and down flows (Graham 1977, Porter & Woodward 1994), demonstrated the role of pressure fluctuations in turning the upflows into downdrafts (Hurlburt et al. 1984), revealed the presence of shocks in the flow (Malagoli et al. 1990, Cattaneo et al. 1990), explored the dependence on parameter space (Cattaneo et al. 1991), investigated the interaction with rotation (Pulkkinen et al. 1993, Brummell et al. 1996, Hurlburt et al. 1996), and clarified the role of boundary layers (Kerr 1996, Julien et al. 1996, Julien & Werne 1997). Other simulations, using realistic stellar physics, have led to a shift in our paradigm for compressible convection, from that of a cascade of energy from large driving eddies to small dissipative eddies, to that of non-local driving by low entropy downdrafts produced on the intermediate scale of granulation by radiative cooling at the extremely thin surface thermal boundary layer, which drive both larger scale cellular flows and smaller scale turbulent motions (Stein & Nordlund 1989; Spruit et al. 1990; Nordlund & Stein 1996; Spruit 1997). Such simulations have also: demonstrated how convective motions alter line profiles (Steffen et al. 1995, Dravins & Nordlund 1990a, 1990b), shown how non-adiabatic pressure fluctuations drive the solar p-modes and how convection alters the mode eigenfrequencies (Stein & Nordlund 1991), revealed that granules are often edge brightened (Stein & Nordlund 1994), disclosed the nature or "exploding granules" (Nordlund 1985), and shown how mass conservation leads to increasingly larger cell structures with increasing depth (Nordlund 1985, Nordlund & Stein 1996). (Also see review by Spruit et al. 1990.)

In this paper, we continue the thread of using realistic physics in simulations to clarify the nature of solar convection, focusing on the near-surface layers. We briefly describe our calculations (section 2) and the mean atmospheric structure that results (section 3). We then discuss the granule dynamics (section 4), energetics (section 5) and evolution (section 6). We compare our results with observations (section 7) and discuss the effects of numerical resolution (section 8). A summary of the main conclusions is given in section 9.

2. Simulation

We simulate a small portion of the solar photosphere and the upper layers of the convection zone, a region extending 6×6 Mm horizontally and from the temperature minimum at -0.5 Mm down to 2.5 Mm below the visible surface. We solve the equations of mass, momentum and energy conservation in the form:

$$\frac{\partial \ln \rho}{\partial t} = -\mathbf{u} \cdot \nabla \ln \rho - \nabla \cdot \mathbf{u} \ , \quad (1)$$

$$\frac{\partial \mathbf{u}}{\partial t} = -\mathbf{u} \cdot \nabla \mathbf{u} + \mathbf{g} - \frac{P}{\rho} \nabla \ln P + \underline{\underline{\tau}} \ , \quad (2)$$

$$\frac{\partial e}{\partial t} = -\mathbf{u} \cdot \nabla e - \frac{P}{\rho} \nabla \cdot \mathbf{u} + Q_{rad} + Q_{visc} \ , \quad (3)$$

where $\underline{\underline{\tau}}$ is the viscous stress tensor, Q_{rad} is the radiative heating and Q_{visc} is the viscous dissipation.

We use a non-staggered grid of $125 \times 125 \times 82$ zones with a short run at higher resolution of $253 \times 253 \times 163$ zones. The spatial derivatives are calculated using third order splines and the time advance is a third order leapfrog scheme (Hyman 1979; Nordlund & Stein 1990). The code is stabilized by a hyper-viscosity which removes short wavelength noise without damping the longer wavelengths:

$$\left(\frac{df}{dt}\right)_{\text{diffusive}} = \sum_i \left(\frac{\partial}{\partial x_i}\right)_+ \left(\nu \alpha \left(\frac{\partial f}{\partial x_i}\right)_-\right) \quad (4)$$

where ν is the numerical viscosity and

$$\alpha = \frac{max_3 \left|\Delta^3 f\right|}{max_3 \left|\Delta f_i\right|} \quad (5)$$

is the hyper-enhancement to the viscosity. Here $\Delta^3 f$ is the third difference, Δf is the first difference of the variable and max_3 signifies the maximum over three adjacent intervals. The viscosity, ν, has three contributions,

$$\nu_i = (c_1 c_{\text{sound}} + c_2 |u_i| + c_3 |\Delta_3^- u_i|) \Delta x_i, \quad (6)$$

where the term proportional to the sound speed stabilizes weak waves, the term proportional to the fluid velocity prevents ringing at sharp changes in advected quantities, and the term proportional to the velocity jump stabilizes shocks. ($\Delta_3^- u$ is the sum of the compressive velocity jumps over 3 zones in each direction.) Our initial state was a snapshot from a lower resolution simulation of the same region (Stein et al. 1988).

A large fraction of the internal energy is in the form of ionization energy near the solar surface, so we use a realistic equation of state (including the effects of ionization and excitation of hydrogen and other abundant elements and the formation of H_2 molecules). The pressure is found by interpolation in a table of $P(\ln \rho, e)$ and its derivatives which is calculated with the Uppsala stellar atmosphere package (Gustafsson et al. 1975). The interpolation is intermediate between bicubic and biquadratic (cubic along each axis).

Radiative energy exchange is critical in determining the structure of the upper convection zone. Near the surface of the sun, the energy flow changes from almost exclusively convective below the surface to radiative above the surface. The interaction between convection and radiation near the solar surface determines what we observe and produces the entropy fluctuations that lead to the buoyancy work which drives the convection. Hence, the interaction between convection and radiation is crucial for both the diagnostics and the dynamics of convection. Since the top of the convection zone occurs near the level where the continuum optical depth is one, neither the optically thin nor the diffusion approximations give reasonable results. We therefore include 3D, LTE radiation transfer in our model. The radiative heating rate

$$Q_{rad} = \int_\lambda \int_{\mathbf{\Omega}} \kappa_\lambda (I_{\lambda,\mathbf{\Omega}} - S_\lambda) d\mathbf{\Omega} d\lambda \ , \quad (7)$$

is found by solving the Feautrier equation along a vertical and 4 straight inclined rays, after averaging the Planck function into four bins by wavelength sorted according to opacity (Nordlund 1982; Nordlund & Stein 1990; Nordlund & Stein 1991a). We make the further approximation that all the opacities scale together, which is reasonable for most continua and lines, except for the numerous weak iron lines. The opacity and source functions are also calculated with the Uppsala atmosphere package.

We can not simulate the entire convection zone (including all the length scales from granulation to the depth of the entire zone). Current computers have neither the memory nor the speed to perform such a calculation for the $\sim 10^5$ years of solar time needed to achieve thermal relaxation throughout the convection zone. We choose to simulate only a small region near the solar surface and must therefore impose boundary conditions inside the convectively unstable region. What happens outside our computational domain in principle influences the convective motions inside. However, at the top boundary, the density is very low relative to the rest of the volume (see Fig 1) and hence whatever happens there has very little influence on the convective motions. At the bottom, the incoming fluid is to a very good approximation isentropic and featureless, and hence carries little information. The unknown influence of external regions should therefore be small. This assertion is indeed confirmed by experiments with boundaries located at different depths.

The horizontal directions are taken to be periodic. In the vertical direction, we have a transmitting boundary at the temperature minimum (Nordlund & Stein 1990). This is achieved by a larger than normal zone at the top boundary. Across this zone we make the vertical derivative of the density hydrostatic, set the vertical derivative of the velocity zero and hold the internal energy at the top fiducial layer constant in time and space. At the bottom of the computational domain, outgoing fluid goes out with whatever properties it has. For incoming fluid, we adjust the pressure such that the net mass flux through the bottom boundary vanishes. (This ensures that there is no boundary work done on vertical oscillation modes.) The pressure on the bottom boundary thus varies in time but is uniform over the horizontal plane. We damp fluctuations of the horizontal and vertical velocity of the incoming fluid, using a long time constant. Finally, we adjust the density and energy of the incoming fluid, at constant pressure, to fix its entropy (in both space and time).

The top boundary conditions were checked by looking at the reflection of acoustic and gravity waves, which is small. The bottom boundary conditions were checked by comparing the properties of this shallow run with those of a much deeper run. We found no statistically significant differences in the convection.

The ability to calculate a wide enough range of length scales to match the dimensionless parameters – Reynolds number, Rayleigh number and Prandtl number – of the solar convection zone is also beyond the speed and memory capabilities of current computers. Thus, our simulations are of the type called "Large Eddy Simulations". It is, however, possible to resolve the surface thermal boundary layer of the convection zone and this we have done. Indeed, this is required to achieve results that agree quantitatively with solar observations.

3. Mean Atmosphere

The mean atmosphere, averaged over horizontal planes and time, is shown in Fig 1. We take z increasing inward and the solar surface, $\langle\tau\rangle = 1$, is at z=0. Between the top boundary, the surface of optical

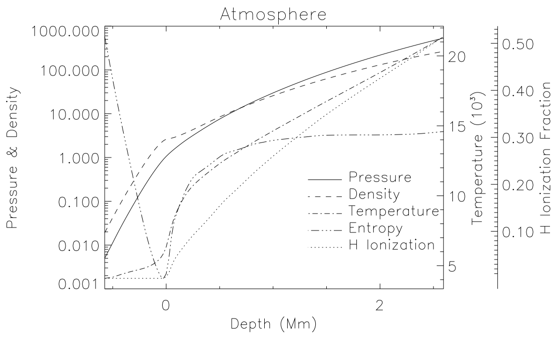

Fig. 1.— Mean atmosphere of the simulation, from the temperature minimum at -0.5 Mm down to 2.5 Mm below the visible surface inside the convection zone. The photosphere is stably stratified. At the top of the convection zone is the highly superadiabatic layer, below which the atmosphere becomes nearly adiabatic. The top 6 pressure scale heights of the convection zone are included in the simulation domain.

depth unity, and the bottom of the computational domain the pressure increases by a factor of 0.005:1:450 (5 + 6 pressure scale heights), the density increases by factors $\approx$ 0.01:1:100, and the temperature increases from about 4000 K through 6000 K to 21,000 K. In the deeper layers the entropy is nearly constant and the temperature gradient is close to adiabatic. Near the surface, the mean entropy gradient steepens and becomes extremely large, in what is called the superadiabatic region, where the average temperature jumps from 6000 K to 10,000 K over 250 km. In the nearly isothermal photosphere the entropy increases outward.

4. Granule Dynamics

4.1. Flows and Shocks

The flow in granules resembles the flow in a gently flowing fountain. Fluid gushes up inside the granule and then flows out towards and over its edge (Figs 2 and 3). Because of the small density scale heights in the visible photosphere, the flow above a granule has to be strongly horizontally divergent in order to conserve mass. Thus a typical fluid parcel quickly obtains a predominantly horizontal velocity and flows towards to periphery of the granule, where it "collides" with the corresponding outflow from the neighboring granule (Fig 4).

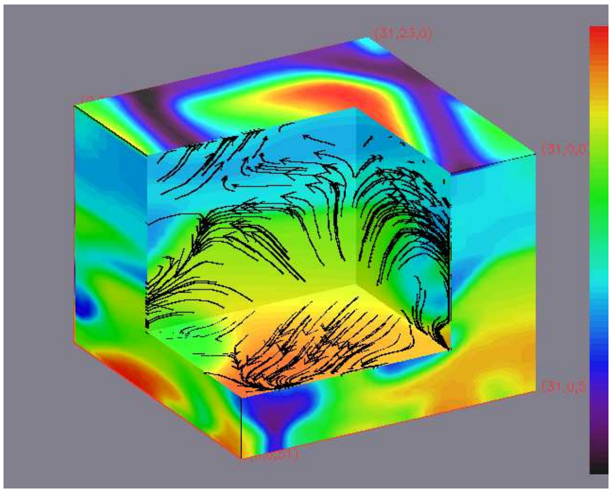

Fig. 2.— An individual granule with a corner cut away to show the velocity field and the temperature structure. A granule resembles a fountain with warm fluid rising up near the center, cooling rapidly as it crosses the optical surface, diverging horizontally, losing its buoyancy and being pulled back down by gravity in the intergranular lanes where large shear produces high vorticity.

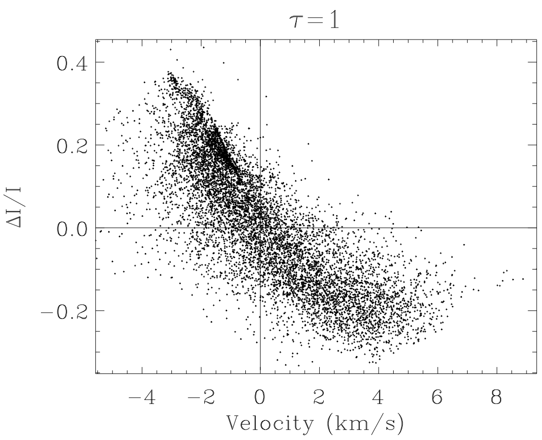

Fig. 3.— Correlation of intensity and vertical velocity at $\tau = 1$. The dark intergranular lanes are downward moving fluid (positive velocity) and the bright granules are upward moving fluid (negative velocity).

In terms of dynamics, the outflow occurs partly because the fluid inside the granule is warmer and hence has a larger hydrostatic pressure scale height than in the intergranular lanes, and partly because dynamic pressure fluctuations develop to enforce mass conservation; this enhances the pressure at the center of granules *and* at the center of the intergranular lanes, relative to the periphery of the granules, where the largest horizontal velocities occur (Fig 4). (See also the discussion of mass conservation in the section on granule evolution.) In the simulations, additional deceleration is provided by the viscous stresses, because the deceleration occurs over just a few grid points. In the intergranular lanes gravity accelerates the fluid downward. Vertical and horizontal velocities as a function of depth are shown in Fig 5.

Occasionally, the horizontal flows reach supersonic velocities and are halted in vertically oriented, nearly stationary shocks at the edges of the intergranular lanes (Fig 6) (Malagoli et al. 1990, Nordlund & Stein 1991b, Nesis et al. 1992, Solanki et al. 1996). These shocks heat the fluid but do not increase its density, because gravity pulls down the denser material which falls out the bottom. The shocks at the edges of intergranular lanes are, however, a rare occurrence. At any one time, supersonic flow occurs in only $\sim 3-4\%$ of the surface.

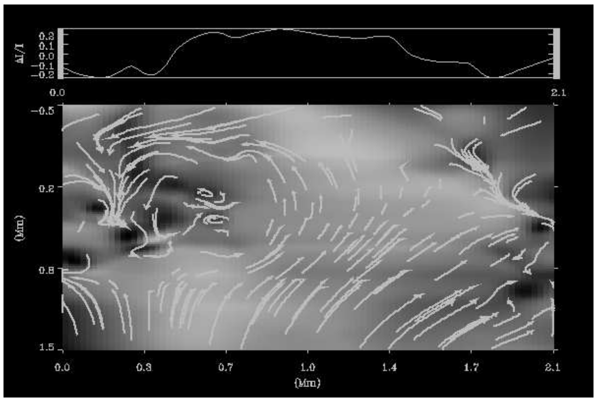

Fig. 4.— Pressure fluctuations about the mean hydrostatic equilibrium and the velocity field in an xz slice through a granule. The pressure is high above the centers of granules, which decelerates the warm upflowing fluid and diverts it horizontally. High pressure also occurs in the intergranular lanes where the horizontal motions are halted and gravity pulls the now cool, dense fluid down into the intergranular lanes. Horizontal rolls of high vorticity occur at the edges of the intergranular lanes. The emergent intensity profile across the slice is shown at the top.

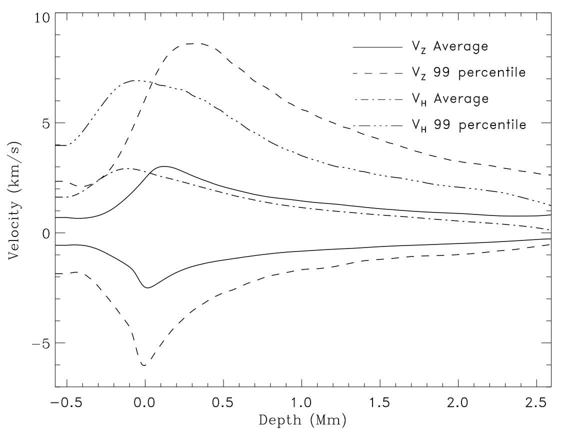

Fig. 5.— Upflow (negative) and downflow (positive) velocities (average and 99^{th} percentile extreme values), as a function of depth. Below the surface the up and downflows are asymmetric, with large downflow but small upflow velocities. Above the surface the horizontal velocities are larger than the vertical velocities.

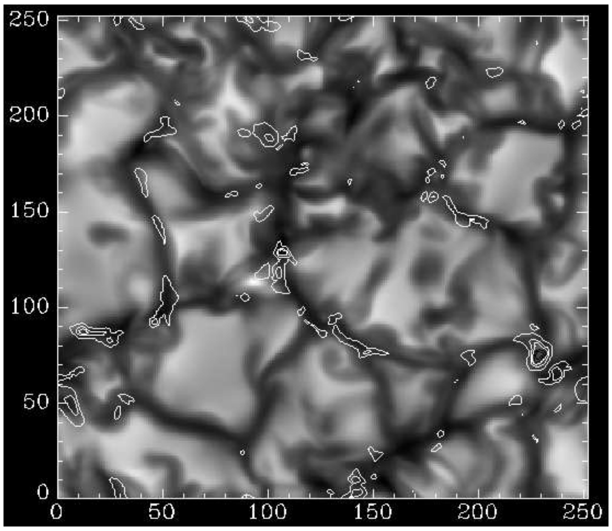

Fig. 6.— Contours of fluid Mach number > 1 near the Solar surface superimposed on an image of the emergent intensity. Supersonic flows occasionally occur just before the horizontally moving fluid is decelerated in shocks at the edges of the intergranular lanes and in downdrafts within intergranular lanes. The axes are the grid index. Each cell is 24 km.

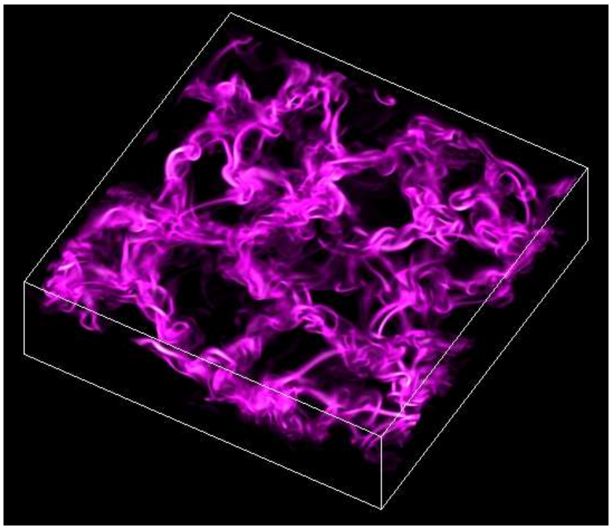

Fig. 7.— Magnitude of the vorticity showing vortex tubes, viewed from above the surface. Granule centers are clear of vorticity which is concentrated in the downdrafts. Twisting of the vortex tubes about each other shows the turbulent nature of the flow.

4.2. Vorticity

Where the flow turns down at the intergranular lanes, pairs of whirls of high horizontal vorticity occur (Figs 4, 7). With increasing resolution these become more turbulent, as can be seen by the complex intertwining of the vortex tubes. There is little vorticity in the granule interiors (visible as the holes in Fig 7).

The source of the vorticity can be quantified by evaluating the equation for the vorticity,

$$\begin{aligned} \frac{\partial \omega}{\partial t} &= -(\mathbf{u} \cdot \nabla)\omega - \omega \nabla \cdot \mathbf{u} + (\omega \cdot \nabla)\mathbf{u} \\ &\quad - \nabla \left(\frac{P}{\rho} \right) \times \nabla \ln P + \nabla \times \nabla \cdot \tau \ . \end{aligned} \quad (8)$$

The first term on the right hand side is advection, the second is vortex stretching, the third is vortex tube tilting, the fourth is baroclinicity, and the last is viscous diffusion. Note that the vortex stretching term $-\omega \nabla \cdot \mathbf{u} = \omega D \ln \rho / Dt$, which shows that vorticity suffers dilution in upflows and concentration in downflows.

The primary source of vorticity is the baroclinic term. It becomes large near the edges of granules, where the two gradients are large and non-parallel. Inside granules, on the other hand, the two gradients are very nearly parallel, because of the nearly isentropic conditions there. In downdrafts, small scale entropy fluctuations occur and hence the baroclinic term is of importance there as well.

In summary then, vorticity is weak in the updrafts because the source term is weak, because the vorticity is diluted with time in proportion to the decrease of the density following the ascending motion, and because overturning fluid advects vorticity into the downdrafts. The vorticity is strong in the downdrafts because vorticity is generated at the granule edges and in the downdrafts proper by the baroclinic term, and because the vorticity is concentrated with time in the downdrafts as the density increases following the motion. Similar conclusions were reached by Nordlund et al. (1997).

As in numerical simulations of isotropic turbulence (e.g., Vincent & Meneguzzi 1994), vorticity tends to concentrate in tube-like structures, whose widths are comparable to the numerical resolution. However, what appears in these renderings to be classical vortex tubes are in fact often structures that have a quite different local flow topology, because strong flows (both horizontal and vertical) are superposed on top of the vorticity. The peaks in vorticity, at least near the surface, are associated with the strong shear that occurs where horizontal flows are deflected downwards into the intergranular lanes. Even in our highest resolution runs, only a small fraction of trace particles released in the flow get caught in a vortex. They spiral around these vorticity maxima at most a few times, contrary to the typical case of vortex tubes in isotropic turbulence. However, since the width of vortex tubes scales with the numerical grid size, when the resolution is increased, the width decreases and the peak vorticity increases. This implies that for higher numerical resolution, one would see the fluid spiral a larger number of times around the vortex tubes.

Another crucial point is to what extent fluid is recirculated back to the surface from the downdrafts, and whether or not the answer is sensitive to the numerical resolution. We find that very little fluid is recirculated back to the surface, independent of numerical resolution. This may appear surprising, in light of the turbulence that develops in the downdrafts at the highest resolutions. One could suspect that some of this turbulence might be fed back into the updrafts, and cause some recirculation of fluid back to the surface. The reason this does not happen is that, after fluid has descended a few hundred kilometers, the regions of descending fluid become well separated from those regions of the ascending fluid that travel all the way to the surface, and thus there is very little return flow to the surface from these layers. This is illustrated nicely by Fig. 4 in Stein & Nordlund (1989), where it is obvious that the tiny fraction of the ascending flow at depth that will eventually reach the surface typically comes from somewhere near the center of an updraft, and is thus separated from the turbulent downdrafts by a region of horizontally divergent flow.

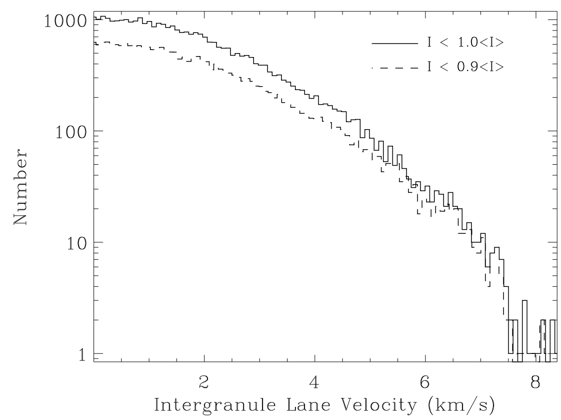

Fig. 8.— Histogram of horizontal flow velocity along intergranular lanes at optical depth unity. Velocity is perpendicular to the gradient of the intensity for those locations where the intensity is less than 1.0 and 0.90 times the average intensity. The distribution is exponential.

4.3. Downflows

Granules sit on top of broader upflows, the mesogranulation, which originate deeper down where the scale height is larger. Penetration of the downflowing intergranular fluid is shallow (≈ 0.5 Mm) around most of the lane. It is halted by the upflow from below. The vertical downflows occasionally become supersonic. Where such downdrafts encounter the upflows they are decelerated at horizontal, subsurface shocks (Fig 4). The pressure fluctuations associated with the shocks drive waves away from where the streams crash into each other.

The fluid whose descent is halted flows horizontally

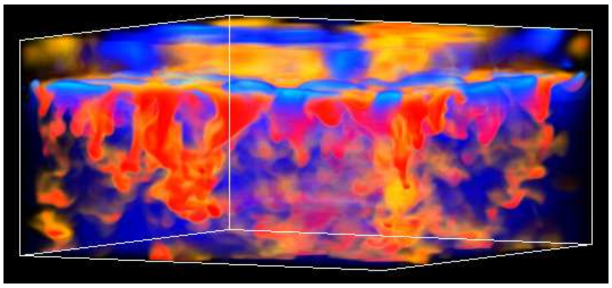

Fig. 9.— Entropy fluctuations, normalized to the same magnitude at all depths, viewed from below the surface. Blue shows high entropy upflows and red and yellow show low entropy downflows. The low entropy filamentary downdrafts twist around as a result of their vertical vorticity, yet penetrate through the entire computational domain.

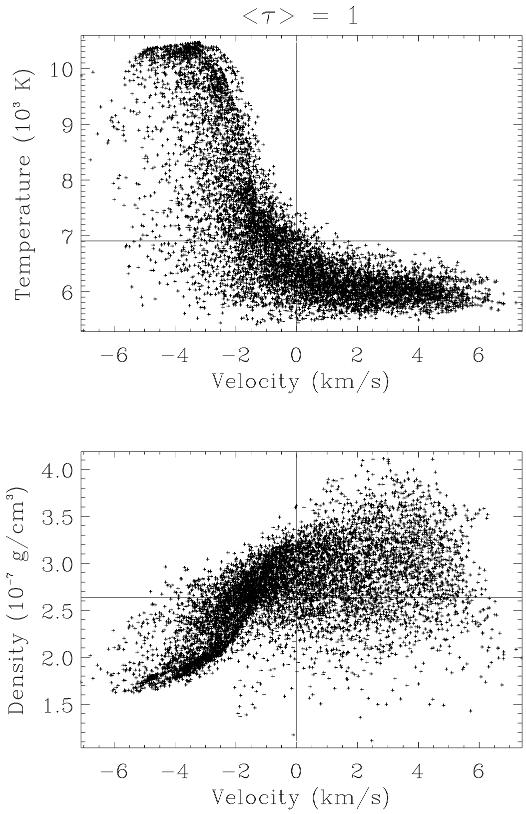

Fig. 10.— Correlation of temperature and density with vertical velocity at geometrical depth where $\langle\tau\rangle = 1$. The distributions are bimodal: granule upflows (negative velocity) have high temperature ($\sim 10^4$ K) and low density, while intergranular downflows (positive velocity) have low temperature (~ 6000 K) and high density. The entropy correlation is similar to the temperature. At a given geometrical depth there is a wide spread in properties because the optical depth in the hot granules and cool intergranular lanes is very different. At given local optical depth, the correlation is one-to-one and tighter (see fig 11).

along the intergranular lanes, as along a trough, toward convergence points which typically occur at the vertices of several granules. We calculate the velocity along the intergranular lanes at $\tau = 1$ by first interpolating the velocity to the level of local unit optical depth, then taking its component perpendicular to the gradient of the intensity and finally selecting only those locations with less than average intensity. Its average value is 1.9 km/s and it has an exponential distribution (Figure 8).

At the convergence points the low entropy fluid forms high velocity downdrafts, which penetrate many scale heights (Fig 9). The heads of the downdrafts are surrounded by a ring of horizontal vorticity where they push aside the ascending flow. A pair of vertical vortex tubes are shed that link the ring vortex at the head of the downdraft back to the surface.

On a somewhat larger scale, convergence is towards particularly strong downdrafts, associated with the meso-granulation. Where these downdrafts occur, the granules tend to be smaller and to move laterally into the downdraft. Over the broad meso-granular upflows the granules tend to be larger. This behavior is confirmed by local correlation tracking of observed granules (Muller et al. 1992).

5. Granule Energetics

We now consider the thermodynamic properties of granulation in relation to the granule structure. The temperature of the plasma is controlled by the balance between convective transport and radiative losses.

5.1. Upflows and Downflows

The temperature, entropy and density of the plasma near the solar surface have approximately bimodal distributions. The downward moving intergranular lane plasma has low temperature, low entropy, very low ionization, and high density. The upward moving granule plasma has high temperature, high entropy, high ionization and low density (Figs 10 and 11). The

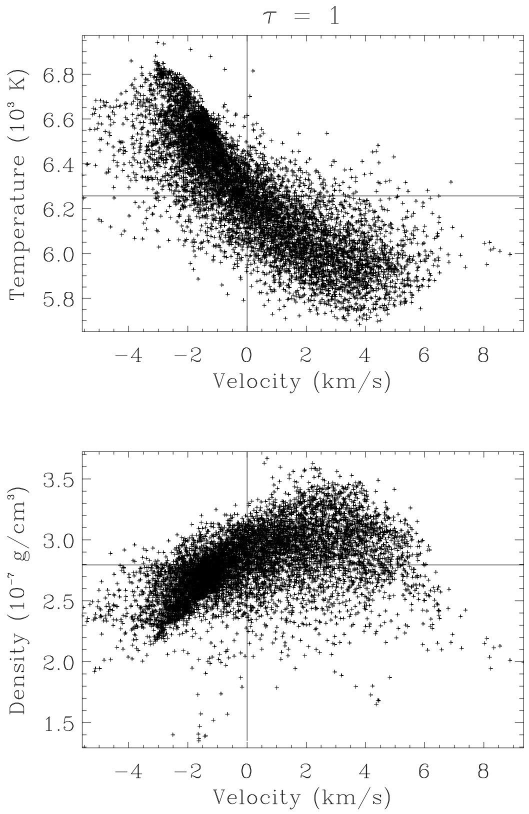

Fig. 11.— Correlation of temperature and density with vertical velocity at local optical depth $\tau = 1$. Granule upflows have high temperature and low density, while intergranular downflows have low temperature and high density. The entropy correlation is similar to the temperature. There is a tighter correlation at given optical depth than geometrical depth because the thermal structure at each point on the Sun is approximately in instantaneous radiative – convective equilibrium.

temperature, entropy and ionization are closely coupled. Below the surface upflows occupy $\sim 2/3$ of the area and downflows $\sim 1/3$. One result of these bimodal distributions is that the edges of granules are extremely sharp with very steep gradients in temperature, entropy and hydrogen ionization. Fig 12 shows the temperature and emerging intensity along a horizontal slice through two granules. Note that granule edges are much steeper in temperature at a given geometric depth than in emergent intensity.

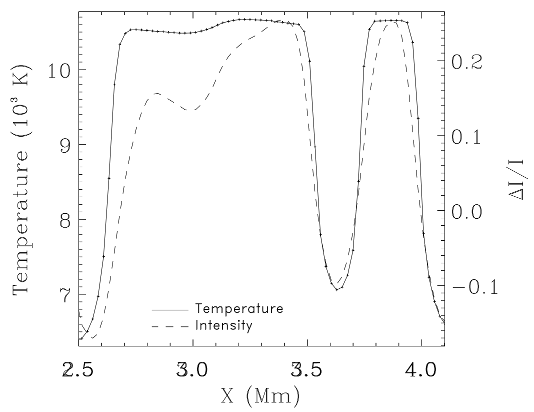

Fig. 12.— Gas temperature and emergent intensity along a slice through the simulation domain at $\langle\tau\rangle = 1$. Note the extremely large temperature gradients at the sides of the granules and the brightness maximum at the edge rather than the center of the larger granule.

5.2. Entropy Structure

Below the surface, the entropy is very nearly constant in the ascending fluid, while it is highly fluctuating in the descending fluid (Fig. 9). The entropy fluctuations in the descending fluid are initiated at the surface, where fluid that visits the photosphere along different paths are cooled by different amounts. While descending, the cold fluid is highly turbulent, and is being mixed with overturning, higher entropy fluid, increasing the fraction of the mass that comes from fluid that overturns without having visited the surface. Thermal diffusion with their higher entropy surroundings also heats the filamentary downdrafts. The mean entropy of the descending fluid thus increases steadily with depth (Fig 13).

5.3. Temperature Structure

Near the surface, the divergence of the convective, radiative and kinetic energy fluxes are large, but the sum of the divergence of all three is small, and vanishing on the average (if exotic terms such as viscous flux are neglected). The radiation cooling time near the solar surface is very short (of order of seconds) so the fluid energy balance adjusts very rapidly. Since the dominant H^- opacity is very temperature sensitive ($\approx T^{10}$), it produces an extremely steep vertical temperature gradient near the surface (Fig 14). The

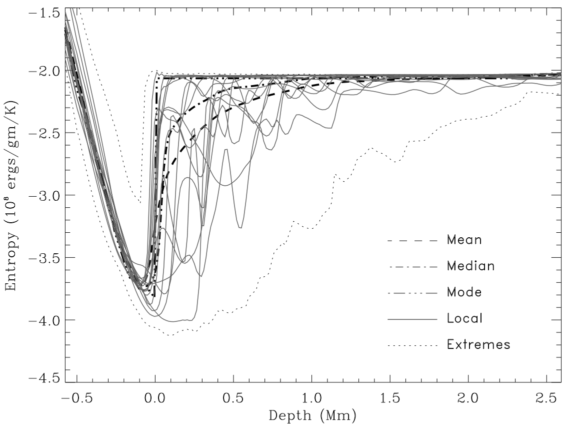

Fig. 13.— Entropy as a function of depth at several horizontal locations plus the average, median, modal and extreme values. Except very near the surface, most of the entropy fluctuations occur in the downdrafts. The range decreases with depth due to entrainment, mixing and thermal diffusion.

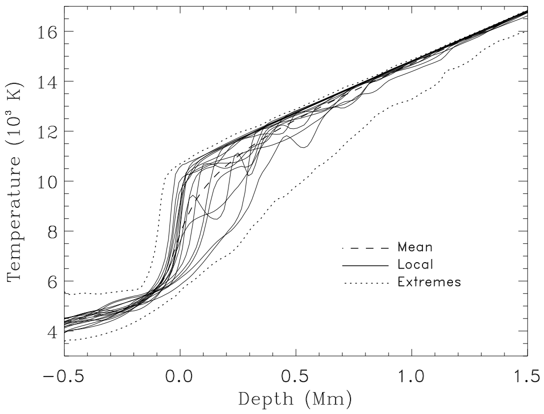

Fig. 14.— Temperature as a function of geometric depth at several horizontal locations plus the average temperature profile. Locally the temperature profile is much steeper than the average profile.

temperature gradient is much larger in the ascending flow ($\sim$ 100 K/km) than in the mean structure ($\sim$ 30 K/km). The smaller value for the average gradient comes about because the steep temperature drop in ascending flows occurs at different depths in different granules, and because the temperature rise in the downdrafts occurs at larger depths and is more gradual than in the updrafts.

Above the surface, the fluid is nearly in radiative equilibrium, with a little radiative heating balancing expansion cooling over granules and a little radiative cooling balancing compressional heating in the converging flow over the intergranular lanes. Changes due to the convective motions are a small perturbation on this basic structure.

Energy transport switches from convective below the surface to radiative above the surface. The fluid is always approximately in radiative – convective equilibrium for the atmospheric structure through which it is moving. The upflows transfer their internal energy to radiation between optical depths $\tau \sim 30$ and $\tau \sim 1$. Between those depths they have a temperature gradient close to but slightly less than the grey radiative equilibrium value of $T \propto \tau^{1/4}$ (Fig 15). Their temperature gradient is slightly less than the radiative equilibrium value because the radiative flux is increasing as the optical depth decreases due to the transfer of energy from convection to radiation. This well known gradient on an optical depth scale corresponds to an extremely steep gradient on a geometric depth scale (Fig 14), because of the extreme temperature sensitivity of the dominant H^- opacity, so that a small increase in temperature produces a large increase in opacity and hence a large increase in optical depth over a very small geometrical depth range. (A Lagrangian perspective, following a fluid parcel, of this Eulerian behavior, is presented at the end of this section.) As a result, there is a much wider spread in temperatures ($\sim$ 5,000 K) at a given geometric depth (just below the surface) (Fig 14) than there is on a local optical depth scale (Fig 15). This clearly reveals the crucial role of radiation in controlling the structure of the solar surface and the closeness of the atmosphere at each point on the surface to instantaneous radiative equilibrium near local optical depth unity. Thus, even though it is tempting to believe that plasma is monotonically cooling as it overturns in the visible photosphere, that is not a correct picture. The overturning plasma is actually close to radiative equilibrium at all times, and is often being heated, rather than cooled, by radiation as it traverses the optically thin layers.

5.4. Energy Fluxes

Near the surface, upflows and downflows transport approximately equal amounts of energy. With

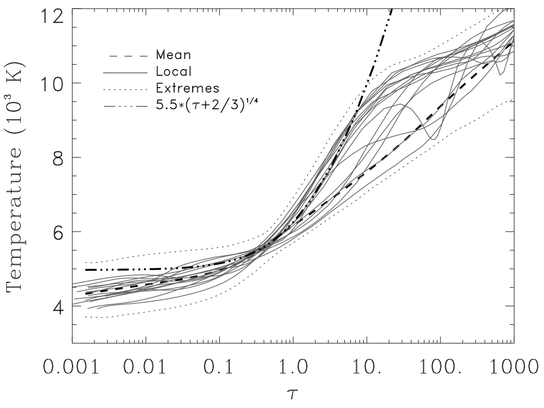

Fig. 15.— Temperature as a function of optical depth at several horizontal locations plus the average temperature profile. On an optical depth scale, the temperature profile is nearly the same at all places in the simulation domain, whether in warm upflows or cool downflows. Thus, the temperature structure is nearly in radiative – convective equilibrium everywhere on the solar surface.

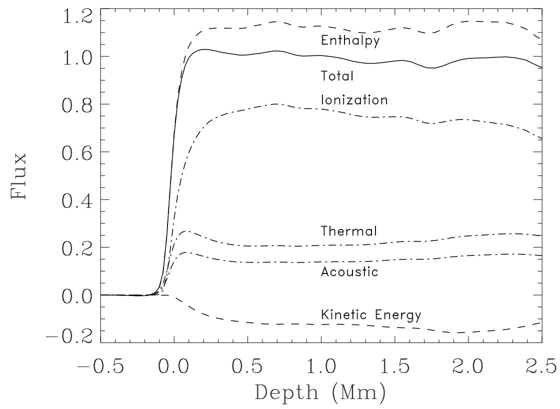

Fig. 16.— The average thermal, ionization, acoustic, and kinetic fluxes plus their sum, the total energy flux, as a function of depth. The thermal plus ionization energy fluxes together are the internal energy flux (not plotted), and this plus the acoustic flux constitutes the enthalpy or convective flux. The enthalpy flux plus the kinetic energy flux is the total energy flux transported by fluid motions. (The viscous flux is very small.) Energy is transported upward through the convection zone near the surface mostly as ionization energy ($\sim 2/3$) and thermal energy ($\sim 1/3$). The kinetic energy flux is downwards and is 10–15% of the total flux.

increasing depth the downflows come to dominate the energy transport. In the near surface layers, energy is transported primarily as ionization energy, $F_{\rm ionization} = (e - 3/2(P/\rho))(\rho u_z - <\rho u_z>)$, ($\sim 2/3$) and thermal energy, $F_{\rm thermal} = 3/2(P/\rho)(\rho u_z - <\rho u_z>)$, ($\sim 1/3$). The kinetic energy flux, $F_{\rm KE} = 1/2\mathbf{u}^2(\rho u_z - <\rho u_z>)$, is about 10% of the enthalpy flux and transports energy downward in the faster downdrafts (Fig 16).

5.5. Convective Driving

Driving of the convective flows comes primarily from the intergranular lanes and downdrafts. The buoyancy forces driving the convective motions are significantly larger in the downflows than in the upflows, below the surface, because the entropy fluctuations are much larger in the downflows, which contain fluid that reached the surface and lost entropy by radiation (Figs 17, 13). The downflows drive the broad, cellular upflows indirectly, through mass conservation, by displacing the warm, entropy neutral, ascending material. With increasing depth these downflows merge into more widely spaced downdrafts, to form a tree-like structure. Correspondingly, the upflows develop a larger scale quasi-cellular structure with increasing depth (an "inverse cascade"). Alternatively, one can view this as the operation of a "normal" convective instability, where the medium is a plasma permeated by granular scale downdrafts. Because of the cooler downdrafts that are superposed on the isentropic background, the mean state is slightly superadiabatic and hence convectively unstable. This initiates motions in the form of diverging upflows and converging downflows, on scales much larger than the scales of the granular fluctuations.

5.6. History of Typical Fluid Parcels

Tracing the history of a typical fluid parcel (Lagrangian perspective, Fig 18) shows that as it approaches the surface the plasma parcel cools adiabatically until it reaches optical depths $\tau \approx 30 - 100$ where it begins to lose heat to radiation. It cools, its opacity drops and photons can escape more easily, increasing the cooling rate. This is a situation with significant positive feedback. A slight drop in

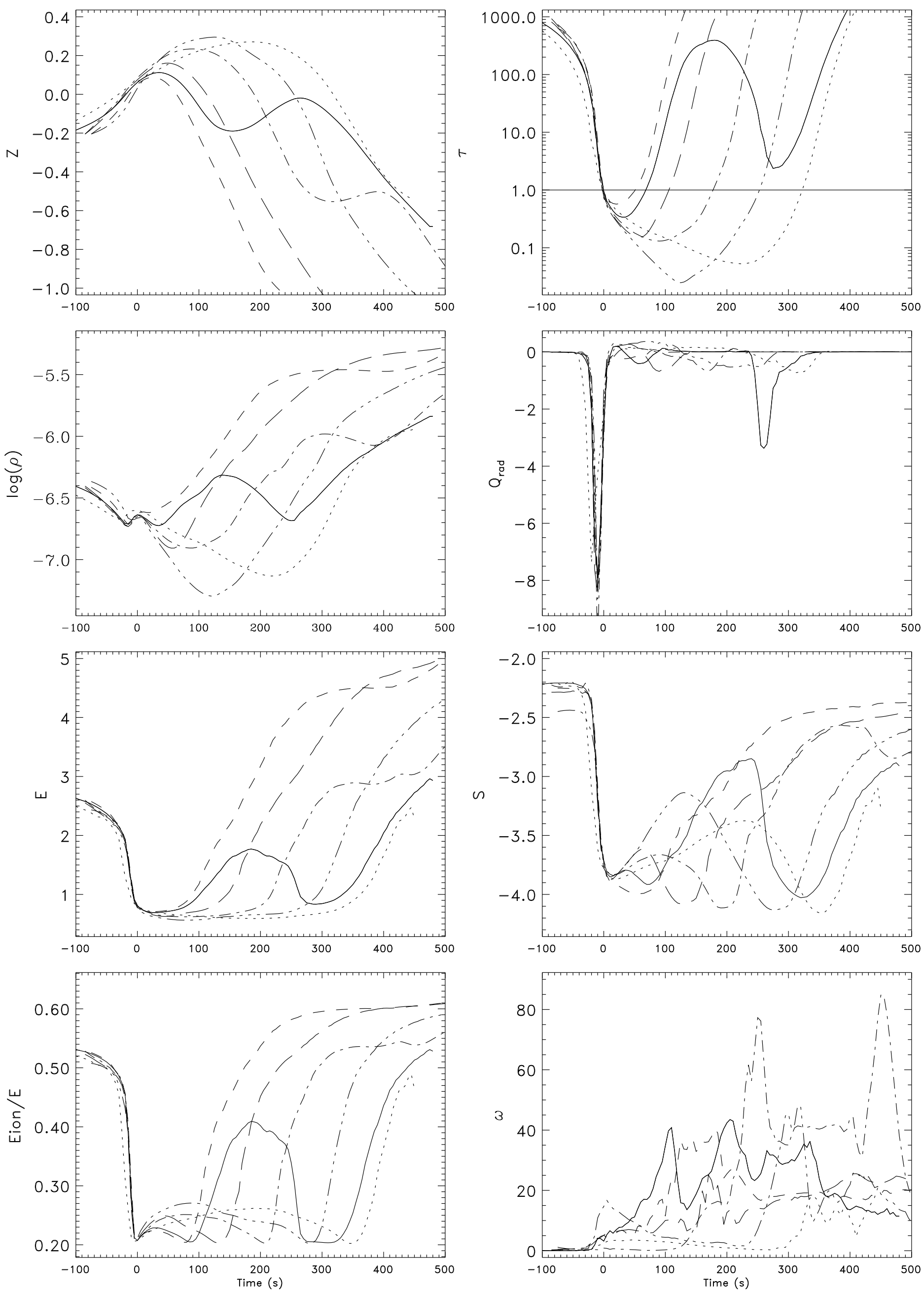

Fig. 18.— Properties of typical fluid parcels that reach the surface, as a function of time: height (Mm), optical depth, $\log(\rho)$, radiative heating (10^3 ergs/gm/sec), energy (10^5 ergs/gm), specific entropy (10^8 ergs/gm/K), fraction ionization to total energy, and vorticity ($10^{-2}\ \mathrm{s}^{-}1$). Time is counted from when the parcel rises through unit optical depth. When fluid reaches optical depth $\tau \sim 100$, it begins to cool rapidly. It recombines. Its entropy and energy drop so quickly that its density increases. As it passes above the surface a small amount of radiative reheating occurs and its entropy increases slightly. When it passes back down through optical depth unity it cools some more with a further drop in entropy. As it heads down into the interior it heats up by adiabatic compression and by diffusive energy exchange. The deeper it gets, the more adiabatic its motion becomes.

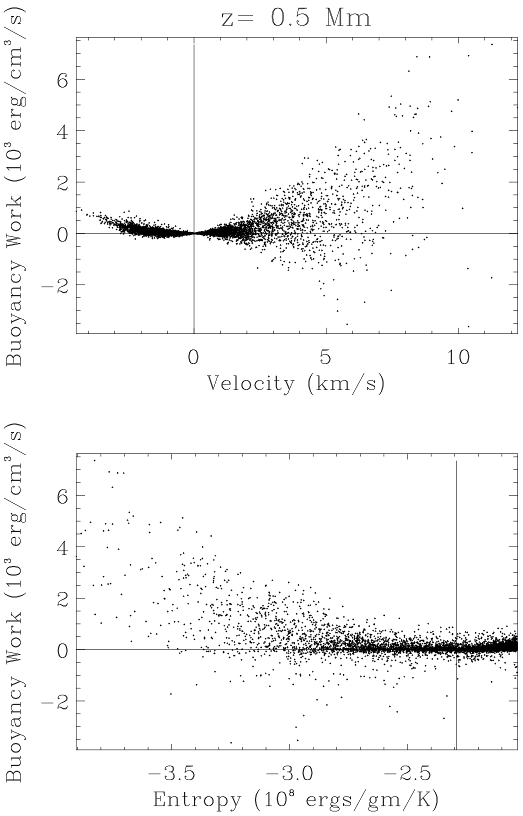

Fig. 17.— Buoyancy work at a depth of 0.5 Mm as a function of (a) vertical velocity and (b) fluid entropy. Most of the convective driving below the surface occurs in the low entropy downflows produced by radiative cooling at the surface.

temperature greatly reduces the dominant H^- opacity and hence the optical depth, so that the radiative loses increase, which further reduces the parcels temperature, and so on. A runaway temperature drop results. Radiation carries away the energy and entropy of the fluid parcel in about 20 sec. An ascending parcel's temperature drop is so rapid ($\sim$ 200 K/s) that its density increases above the average for its depth, whereupon gravity and an adverse pressure gradient (relative to the mean) slow its vertical motion and the high pressure pushes it horizontally. The horizontal deflection shows up as a brief period of large strain without any significant vorticity. The parcel moves along the surface toward an intergranular lane at shallow optical depth for a minute or two. It continues emitting and absorbing radiation, with a small net effect of a little radiative reheating as the fluid passes above a warm granule. This keeps the fluid, which would otherwise cool adiabatically to a very low temperature as it expands into the low density photosphere, at near (but slightly below) the radiative equilibrium temperature. The entropy increases slightly during this period. Parcels that pass through the unit optical depth surface reach heights that average about 200 km and typically stay above the surface for $\approx$ 3 minutes. On reaching a cool intergranular lane, the local radiation equilibrium temperature suddenly drops. The plasma parcel cools, its density increases further and buoyancy pulls it down. The plasma parcel now heads down into the interior. As it turns down it typically passes through a region of both large vorticity and large strain. There is no more radiative heating or cooling during its descent. Unless the parcel is inside a major downdraft, thermal diffusion in the cool intergranular lanes (which become very narrow with increasing depth) raises its entropy as it descends. Eventually, diffusion decreases and the parcel descends with a more gradual increase of entropy. Those parcels in the interior of major downdrafts keep their low surface entropy longer because they do not experience as much diffusive thermal energy exchange.

6. Granule Evolution

Granules evolve because their diverging flow pushes against neighboring granules and because overlying cool fluid splits them apart. Above a granule, high pressure—due to higher temperatures and larger scale height—diverts the flow horizontally, producing a fountain like topology. The horizontal flow encounters surrounding expanding granules against which it pushes. Granules with the largest pressure driving their expansion win the competition and grow, while others with less pressure excess have their growth limited and may even shrink.

To conserve mass, most of the upflow through a granule must flow out through its edge over approximately a scale height, H, hence

$$\pi r^2 \rho v_z \approx 2\pi r H \rho v_H \ . \tag{9}$$

There is a minimum vertical velocity needed to transport sufficient energy to the surface to balance the radiative losses. This can be estimated by balancing the radiative loss from the surface corresponding to the solar flux with the enthalpy flux corresponding to a hydrogen ionization fraction of 10%,

$$\sigma T^4 \approx \rho v_z 0.1\chi \ , \tag{10}$$

where χ is the hydrogen ionization potential. This gives a velocity of ~2 km/s for the minimum needed to supply the radiative losses from the surface (Nordlund & Stein 1991a). Since the vertical velocity can not decrease below this value if the granule is to remain bright, the horizontal expansion velocity must increase as the granule size increases to balance the greater volume of fluid being brought to the surface through the larger granule area,

$$v_H \approx v_z \left(\frac{r}{2H}\right) \ . \tag{11}$$

This relation also sets the maximum horizontal extent of a granule, because horizontal velocities can not be much greater than the sound speed, which varies between 6 km/s in the photosphere and 16 km/s at 2.5 Mm depth. Granules vary in size from a lower limit of unit horizontal optical depth to a maximum size of several times the scale height. To drive this greater horizontal expansion a larger pressure perturbation is needed,

$$\delta P \approx \rho v_H^2 = \rho v_z^2 \left(\frac{r}{2H}\right)^2 \ . \tag{12}$$

Mass conservation takes care of itself by acting through the pressure. If there is insufficient pressure to push enough mass out horizontally, the density builds up over the granule until the pressure is raised sufficiently to expel it. The excess pressure also decelerates the upflow and thus reduces the energy transport to the surface, in particular near the granule center, which then cools. Hence, as granules grow, the upflow velocity near their center decreases and they develop an edge brightened appearance.

Once the ascent velocity drops below the ~2 km/s that is needed to maintain the surface intensity, a mechanism that is reminiscent of an instability sets in. Those locations where the ascent velocity is lowest, and where hence the heating from below is the smallest, are also the locations that cool the most. Their density increases and they experience the most rapid deceleration of the ascent velocity. The decreasing ascent velocity decreases the heating further, and the process eventually leads to a reversal of the vertical velocity. Since the process advances more rapidly at those places where it has already progressed the most; the result is the development of small scale, narrow features; cool spots and lanes, that split granules into fragments.

7. Visible Surface

The emergent intensity in the simulation reveals granules with much sharper, brightened, edges than are observed. However, when the simulation intensity is convolved with a typical point spread function (modulation transfer function), representing the telescope plus the atmospheric seeing, then the simulated and observed granules appear very similar (Fig 19).

Edge brightened granules, which are common in the simulations, are also seen in the highest resolution observations (Keller & Von Der Luehe 1992, Title 1996). The effect is due to the greater vertical velocity and hence heat transport near granule edges (see the discussion of mass conservation in the previous section, and Figs 3 and 4). "Exploding granules" are an extreme manifestation of this effect (Nordlund 1985).

The simulated granule size spectrum (after smoothing) agrees with that of observed granules over the range of resolved sizes (Fig 20). The intensity distribution of the simulated granules (after smoothing) and observed granules is also the same (Fig 21). The rms fluctuation in the frequency integrated emergent intensity is 16% in the raw simulation and 10% after smoothing, which is the same as measured from the La Palma snapshot.

The gas temperature near the solar surface in the simulation shows a large temperature range – from about 5000 K to 10^4 K (Fig 10). However, neither the observed nor the simulated radiation temperature

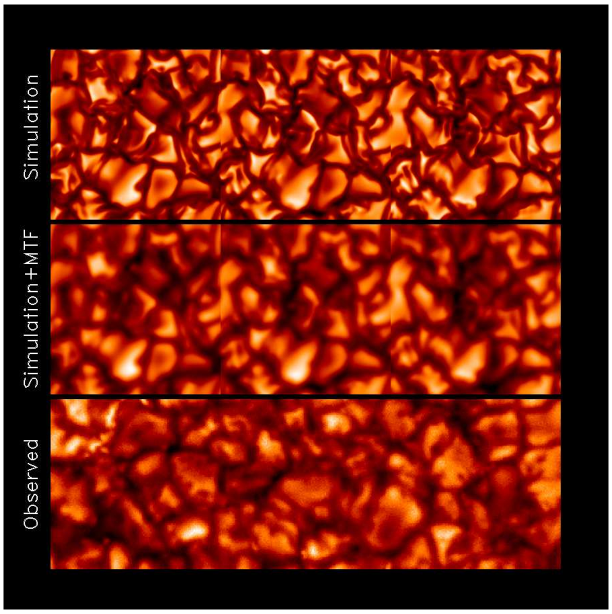

Fig. 19.— Comparison of granulation as seen in the emergent intensity from the simulations and as observed by the Swedish Vacuum Solar Telescope on La Palma. The top row shows three simulation images at one minute intervals, which together make a composite image 18 × 6 Mm in extent. The middle row shows this image smoothed by an Airy plus exponential point spread function (psf). The bottom row shows an 18 × 6 Mm white light image from La Palma. Note the similar appearance of the smoothed simulation image and the observed granulation. The common edge brightening in the simulation is reduced when smoothed. Images by Title (1996) taken in the CH G-band have much more contrast than white light and clearly reveal the edge brightening of granules.

has anywhere near such a large range (Fig 22). The small range of observed intensity fluctuations does *not* imply a small range of gas temperatures at a given geometrical depth. In accordance with the Eddington-Barbier relation, the radiation temperature is approximately equal to the gas temperature at optical depth one (Fig 23). However, the surface on which the continuum optical depth is unity is corrugated with an rms variation of ≈ 30 km from place to place on the visible surface (Fig 24). A given geometrical layer thus represents a wide range in optical depths near $\tau \approx 1$. Properties observed at unit optical depth do not refer to a unique geometric depth, and observers should be cautious in their statements about Doppler

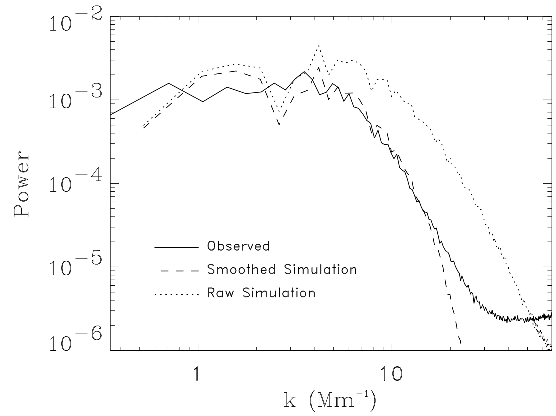

Fig. 20.— Horizontal size spectrum of observed and simulated granules including effects of smoothing by the point spread function.

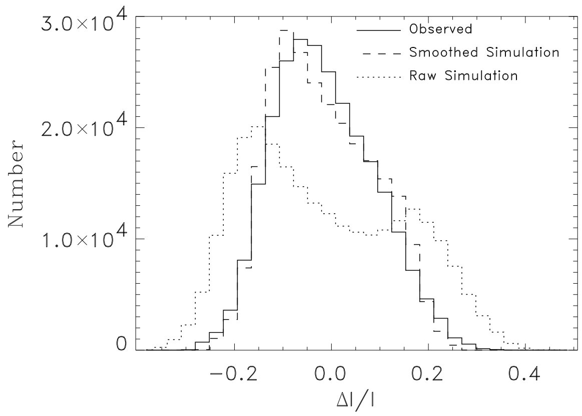

Fig. 21.— Histogram of the emergent radiation intensity from the raw simulation, after smoothing with the psf and from a snapshot of observations made by the Swedish Solar Telescope on La Palma. Note the asymmetric shape and good agreement between the observations and the smoothed simulation.

velocities, temperatures etc. We never see the high temperature gas because it is very opaque. This is a result of the rapid increase in the H^- opacity with temperature, so one looks down to shallower depths in hotter regions and doesn't see the high temperature gas.

The layer from which we observe photons depends on the temperature gradient as well as the tempera-

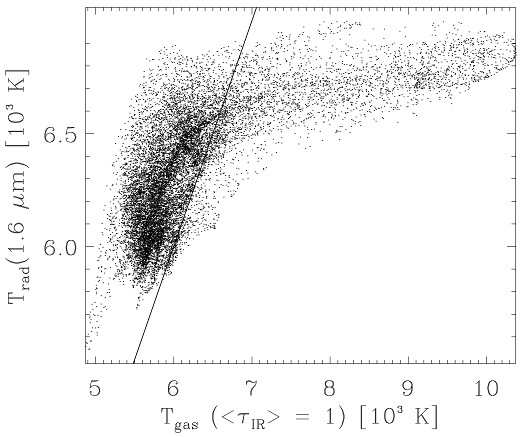

Fig. 22.— Correlation of radiation temperature at 1.6 μm with gas temperature at the depth where $\langle \tau_{1.6\mu m} \rangle = 1$. We never see the radiation from the high temperature gas because it lies at large local optical depth due to the great temperature sensitivity of the H^- opacity ($\kappa \propto T^{10}$).

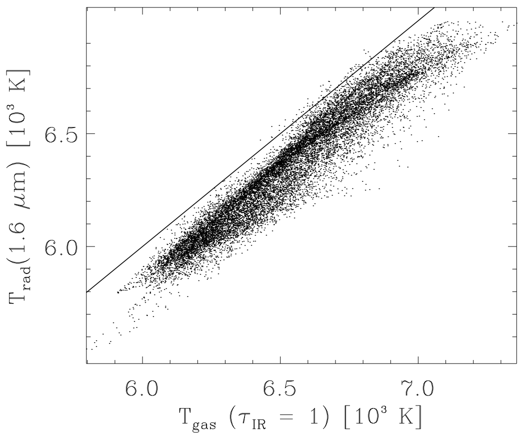

Fig. 23.— Correlation of radiation temperature with gas temperature at the depth where $\tau_{1.6\mu m} = 1$ locally. In accordance with the Eddington-Barbier relations, radiation emerges with temperature approximately equal to the gas temperature at optical depth unity.

ture. Where the temperature gradient is larger, high temperature is reached in a shorter geometric distance, so the optical depth is smaller at a given temperature and hence we observe photons from a slightly deeper layer having a higher gas temperature.

The bright granules are surrounded by dark connected intergranular lanes where the cool fluid is descending back into the sun (Figs 3 and 19). In the low resolution simulation these intergranular lanes often appear quite linear. Increasing the resolution produces more intertwining and twisting in the horizontal vortex tubes along the edges of the intergranular lanes. The simulation also shows many instances of dark lanes cutting through granules and, as discussed in the previous section, this is one way in which granules evolve.

The meso-scale cells several megameters below the surface produce an imprint on the emergent intensity – major intergranular lanes coincide with the location of downdrafts at the cell boundaries (Fig 25). However, this imprint is hard to detect in practice because the intergranular lanes corresponding to the meso-scale cell boundaries do not have any clearly distinguishing features. The subsurface meso-scale cells are most clearly revealed by local correlation tracking which shows the long time scale horizontal flows

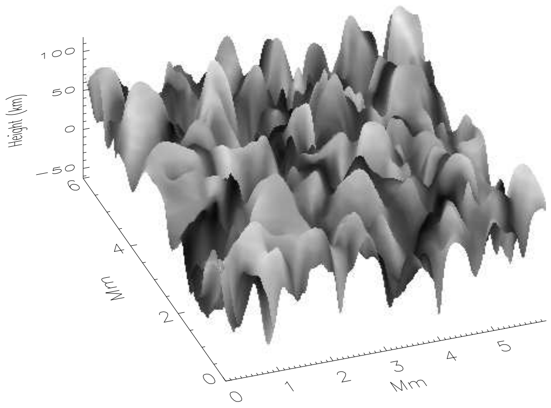

Fig. 24.— Surface of optical depth unity shaded by the gas temperature. The rms height variation of unit optical depth is 30 km. Hot gas reaches unit optical depth higher up and cooler gas deeper down.

(November & Simon 1988) and by following small magnetic elements (Berger et al. 1995).

8. Effects of Numerical Resolution

Convection in the solar surface layers is subject to a number of constraints. Some of these have the

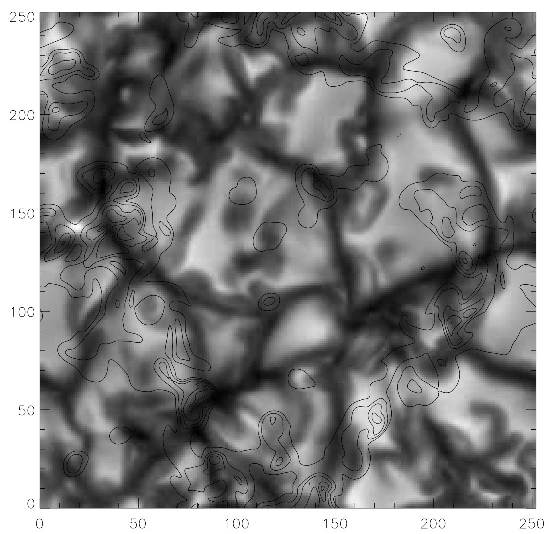

Fig. 25.— Contours of downward velocity at 2 Mm below the surface superimposed on an image of the emergent intensity. The downflow around the edge of the meso-scale cell at 2 Mm coincides closely with intergranular lanes at the surface, but there is no feature that clearly distinguishes these intergranular lanes from all the others.

form of mathematically exact conservation laws, such as for example the requirement that the total energy flux must, on the average, be equal to the nominal solar surface flux. Other constraints are less strict, but are still closely related to fundamental physical conservations laws. One example is the mixing of entropy due to the overturning of ascending fluid. The rate of mixing is determined essentially by mass conservation, and is thus independent of numerical resolution. This renders such statistics as average entropy and temperature as a function of depth very robust (Fig 26). For most practically purposes (p-mode fitting may be an exception), these averages are converged already for the 63^3 model.

Another example was discussed in connection with Eq. 10, where we used the average ionization just below the surface to estimate the required vertical velocities in granules. The difference between different models in the fractional ionization just below the surface is very small, since the entropy of the ascending material is practically independent of numerical resolution. As a corollary, it follows that the average

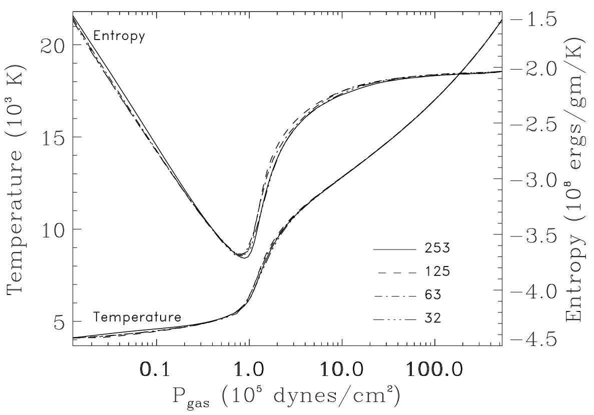

Fig. 26.— Average temperature and entropy as a function of gas pressure for four resolutions: $32^2 \times 41$ $(200\text{km})^2 \times 50 - 140\text{km})$, 63^3 $(100\text{km})^2 \times 35 - 100\text{km})$, $125^2 \times 82$ $((50\text{km})^2 \times 25 - 70\text{km})$, and $253^2 \times 163$ $((25\text{km})^2 \times 15 - 35\text{km})$.

ascent speed in granules is a quite robust quantity. From this it would, however, be premature to conclude that the *distribution* of vertical velocity is insensitive to numerical resolution. Indeed, we show below that, at least in the narrow layer at the surface where the vertical velocity has the widest distribution, the extrema of that distribution are sensitive to the numerical resolution (Fig. 27), and that this sensitivity is reflected in the second order moment of that distribution (the turbulent pressure shown in Fig 28).

Below the surface, the distribution of both entropy and downward velocity are exponential (Figs 27 and 29), reflecting the turbulent mixing of entropy in the downdrafts. As shown by the lower panels of Figs 27 and 29, the bulk of the exponential distributions are converged already at low resolution, but by the very nature of an exponential distribution, the tail never converges. The theoretical distributions cannot be truly exponential, since the fluctuations of both velocity and entropy are bounded, but it appears likely that the theoretical entropy distribution could extend down to the lowest entropy injected at the surface level (see the top panel of Fig. 29).

A comparison of the spectra of, for instance the entropy or velocity, as the resolution is increased shows that they are converged at scales larger than about 8 grid zones (Fig 30). This is quite reasonable, since

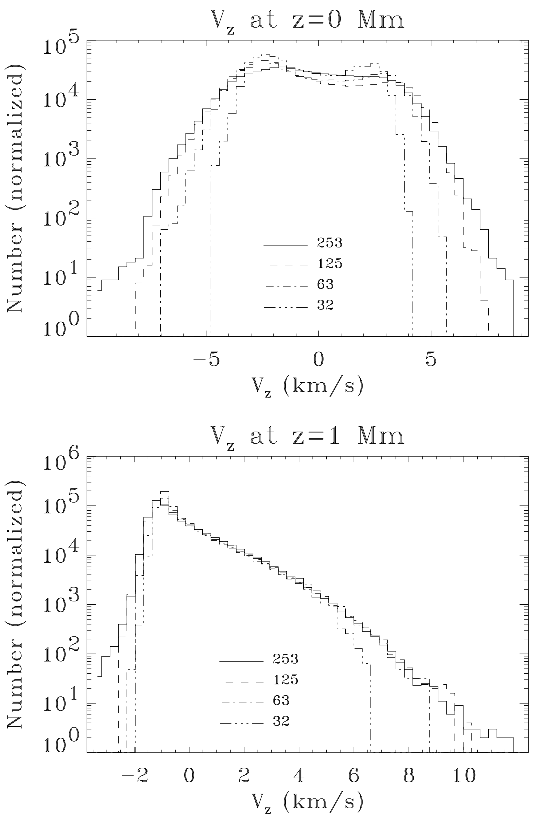

Fig. 27.— Histogram of velocity distribution at the solar surface and 1 Mm below the surface for the same four resolutions as figure 26. Below the surface the distribution is exponential.

our hyperviscosity enhances the diffusion at scales smaller than 6 grid zones and decreases rapidly at larger scales.

Apparent convergence in the spectrum and distribution of a quantity, e.g. the velocity, with increasing resolution does not assure convergence of moments or derivatives of that quantity, e.g. turbulent pressure or vorticity. Moments emphasize the maximum values in the distribution and derivatives emphasize the smallest scales. Some of these quantities have significant observable effects: for example, the turbulent pressure (Fig 28) controls the extension of the atmosphere and hence the p-mode frequencies. Although high vorticity (Fig 31) is often correlated with the dissipative reheating of the downflowing material in the intergranular lanes, the amount of dissipative reheating, which is proportional to the viscosity times the square of the strain, is independent of the resolution.

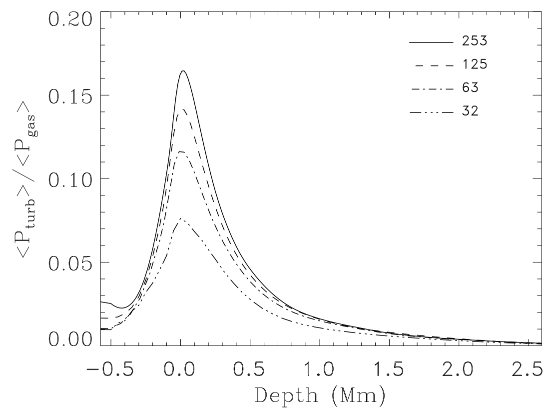

Fig. 28.— Mean turbulent pressure as a fraction of the mean total pressure as a function of depth for the same four resolutions as figure 26. Turbulent pressure is important in extending the mean atmosphere slightly in the superadiabatic layers and above, which lowers the eigenfrequencies of medium and high ℓ modes whose upper turning points lie in this height range.

Another quantity with observable consequences is the Mach number, which controls the turbulent generation of waves. Supersonic Mach numbers occur only at the maxima of the velocity distribution and hence are sensitive to the resolution. The maximum Mach number increases slowly with increasing resolution (Fig 32).

In contrast, the insensitivity of the convective, kinetic energy and radiative fluxes to the resolution (Fig 33), shows that the basic convective structure is already well represented at the resolutions that can currently be achieved in numerical simulations.

9. Summary and Conclusions

Realistic simulations of convection near the solar surface lead to a paradigm shift in our perception of convection. Convection is inherently non-local. It is driven from the surface thermal boundary layer, on the intermediate scale of granulation, by radiative cooling which produces low entropy fluid that descends in the intergranular lanes and merges into deeply penetrating, filamentary downdrafts, which

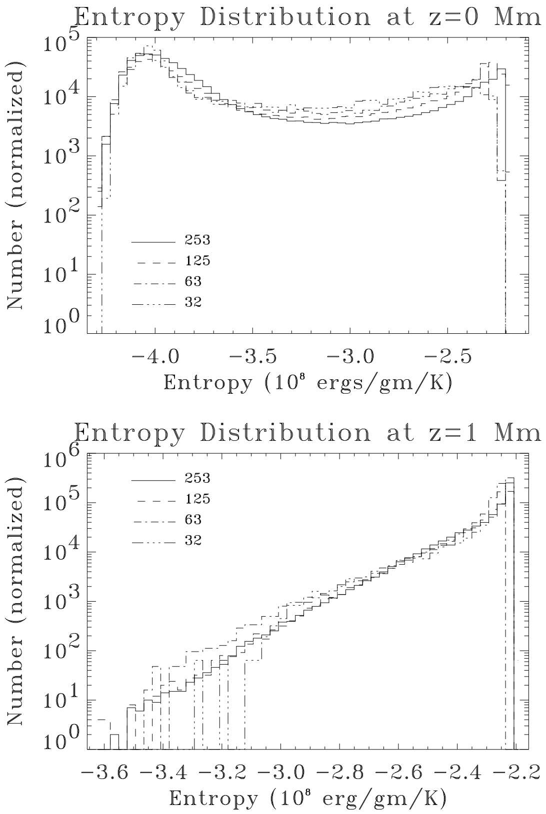

Fig. 29.— Histogram of entropy distribution at the solar surface and 1 Mm below the surface for the same four resolutions as 26.

are the primary site of buoyancy work. These downdrafts drive both larger scale cellular upflows and smaller scale turbulent motions.

The energy carrying granular motions have horizontal sizes that are an order of magnitude larger than the local scale heights. Convective transport is thus very different from the picture that lies behind the traditional local mixing length estimates of convective transport and also much at odds with the assumptions adopted by Canuto & Mazzitelli (1991). This does not necessarily imply that local mixing length scaling relations are completely incorrect; only that if they work qualitatively (as seems to be the case – cf. Trampedach et al. 1997) it is perhaps simply because most fluid must turn over within a scale height in order to conserve mass. The entropy mixing implied by mass conservation is a very robust property, and implies more or less a "mixing length" scaling with the density scale height (see also Nordlund 1975). Indeed,

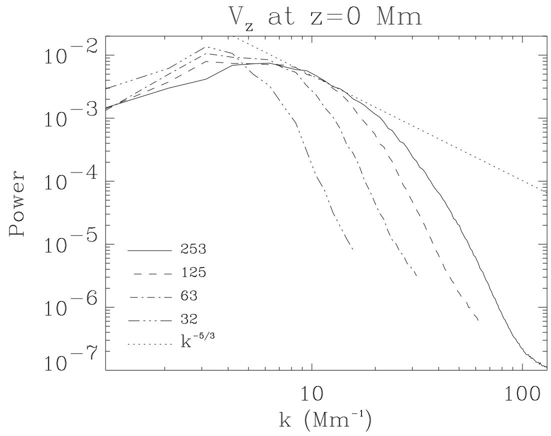

Fig. 30.— Horizontal size spectrum of vertical velocity at the surface for the same four resolutions as figure 26 The dotted line represents a $k^{-5/3}$ power law, however, the simulations do not yet show an inertial range cascade at these resolutions (since the motions are transsonic it is not even clear that an index of -5/3 is to be expected).

Vitense in her early work applying mixing length arguments to stellar convection, did not use the concept of "parcels traveling a distance αH_P", but referred to the inevitable overturning enforced by mass conservation (see Vitense 1953; Böhm-Vitense 1958; Böhm-Vitense 1989).

Hence, convection should be pictured in terms of upflows and downflows, rather than as a hierarchy of eddies. Upflows are warm, low density and entropy neutral. They diverge and overturn, in order to conserve mass as they rise into lower density layers. Only a small fraction of ascending fluid reaches the surface and has its energy and entropy removed by radiation, producing dense material that is pulled down by gravity to form the downflows. Downflowing fluid converges into filamentary structures in order to conserve mass as it descends into higher density layers and it entrains fluid from the overturning upflows. Shear at the downdraft edges creates vorticity and turbulence. Ascending fluid, in contrast, has a very low level of fluctuations, because its divergence smooths out all perturbations. As a result, the upflows appear laminar and the downflows appear turbulent.

The fluid in the upflows ascends nearly isentropically until it reaches continuum optical depth $\tau \sim$ 30 – 100 ($\sim$50 km below optical depth unity), when

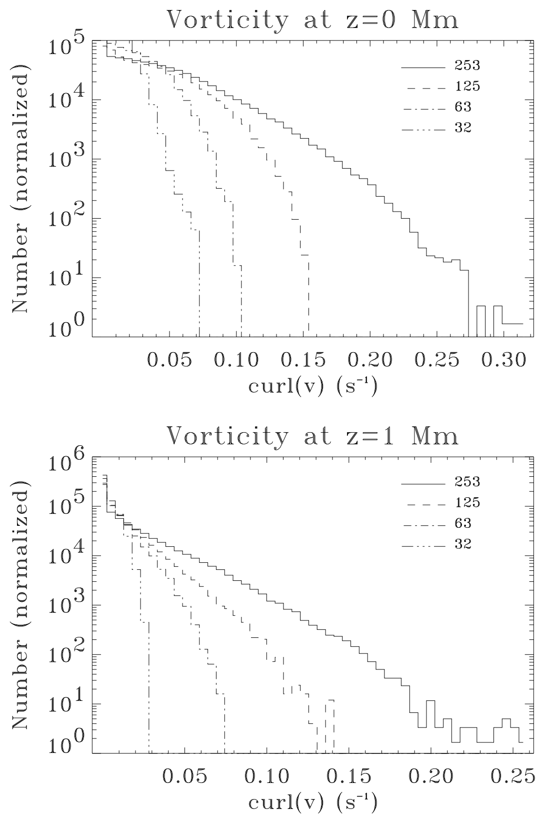

Fig. 31.— Histogram of vorticity at the surface and 1 Mm depth for the same four resolutions as figure 26. Such derivative quantities as vorticity increase with increasing resolution until viscous dissipation scales are reached.

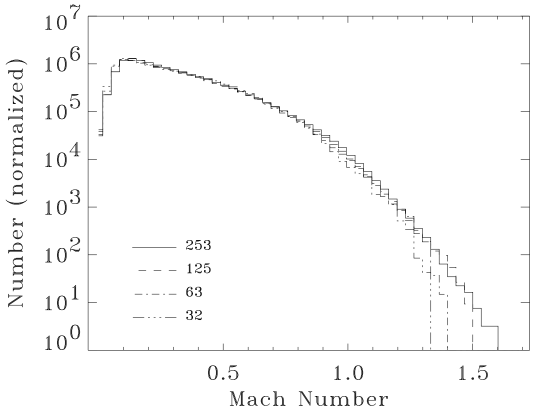

Fig. 32.— Histogram of Mach number distribution for the same four resolutions as figure 26.

photons begin to escape and the fluid begins to cool and lose entropy. This reduces its opacity, so it can cool even faster. A runaway entropy and temperature drop occurs, down to the local radiative equilibrium temperature. Fluid that arcs above the surface of unit optical depth is slightly reheated by radiation (which compensates for its adiabatic expansion cooling) and then when it descends back down through unit optical depth it experiences additional cooling and entropy loss. A typical fluid parcel then heads down into a downdraft, where it encounters strong vorticity and mixing.

Granules evolve by pushing out against and being pushed in by their neighboring granules. As granules expand, the pressure near their center is increased by the ascending flow in order to divert itself horizontally to conserve mass. The enhanced pressure also decelerates the upflowing fluid, thus reducing the heat transport to the surface and producing a stagnation point over the granule. This allows the photosphere above the granule to cool, become denser and be pulled down by gravity, initiating a new dark intergranular lane splitting the original granule.

Observations of the Sun reveal its properties near optical depth unity at the observing frequency. This surface is corrugated, with an rms "roughness" in the continuum of about 30 km. At a given geometric depth near the surface there is a huge range in temperature (~ 5000 K to $\sim 10^4$ K). We never observe such a huge range in radiation temperature, because the dominant H^- opacity increases very rapidly with temperature, so $\tau = 1$ occurs within a narrow range of temperatures. Over hot granules we, thus, view a higher layer than over cool intergranular lanes.

The current convection simulations are robust and, since solar convection is directly observable, they can be compared with observations. Synthetic images and spectra calculated from the numerical simulations reproduce most features of the observations already at current numerical resolution. Observational constraints from spectral line broadening, wavelength shifts, granule size spectrum and intensity distribution are satisfied (Lites et al. 1989). In addition, as will be discussed in future papers, the discrepancy between p-mode observed frequencies and eigenfrequencies of spherically symmetric models is resolved and the driving and damping of the modes is explained. Hence, within the limitations discussed earlier in the

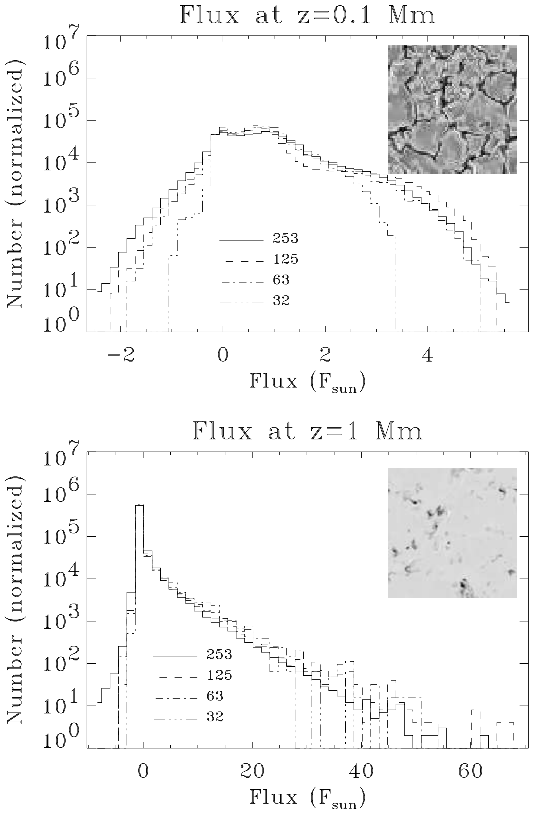

Fig. 33.— Histogram of the total flux at 0.1 Mm and 1 Mm depth for the same four resolutions as figure 26. Images of the flux in a 253 snapshot are also shown, with dark being the largest values. At 0.1 Mm the largest fluxes occur in the intergranular lanes, while at 1 Mm the large fluxes occur in a few isolated downdrafts.

paper, one can use numerical simulations, such as the present ones, to investigate the nature of solar (and stellar) convection.

The work of Å.N was supported in part by the Danish Research Foundation, through its establishment of the Theoretical Astrophysics Center. RFS was supported by NASA grants NAG 1695 and NAG 5-4031 and NSF grant AST 9521785. The calculations were performed at the National Center for Supercomputer Applications, which is supported by the National Science Foundation, at Michigan State University and at UNI•C, Denmark. This valuable support is greatly appreciated.

References

Berger, T. E., Schrijver, C. J., Shine, R. A., Ta rbell, T. D., Title, A. M., Scharmer, G. 1995, ApJ, 454, 531

Berger, T. E., Title, A. M. 1996, ApJ, 463, 365

Böhm-Vitense, E. 1958, Zs. f. Ap., 46, 108

Böhm-Vitense, E. 1989, Introduction to Stellar Astrophysics: vol 3, Stellar Structure and Evolution, Cambridge Univ. Press, Cambridge, UK

Brummell, N. H., Hurlburt, N. E., Toomre, J. 1996, ApJ, 473, 494

Canuto, V. M., Mazzitelli, I. 1991, ApJ, 370, 295

Cattaneo, F., Brummel, N. H., Toomre, J., Malagoli, A., Hurlburt, N. E. 1991, ApJ, 370, 282

Cattaneo, F., Hurlburt, N. E., Toomre, J. 1990, ApJ, 349, L63

Dravins, D., Nordlund, Å. 1990a, A&A, 228, 184

Dravins, D., Nordlund, Å. 1990b, A&A, 228, 203

Duvall, T. L., J., Kosovichev, A. G., Scherrer, P. H., Bogart, R. S., Bush, R. I., De Forest, C., Hoeksema, J. T., Schou, J., Saba, J. L. R., Tarbell, T. D., Title, A. M., Wolfson, C. J., Milford, P. N. 1997, Solar Phys., 170, 63

Graham, E. 1977, in Problems of Stellar Convection, Vol. 71 of *Lecture Notes in Physics*, Springer-Verlag, Berlin, p. 151

Gustafsson, B., Bell, R., Eriksson, K., Nordlund, Å. 1975, A&A, 42, 407

Hurlburt, N. E., Matthews, P. C., Proctor, M. R. E. 1996, ApJ, 457, 933

Hurlburt, N. E., Toomre, J., Massaguer, J. M. 1984, ApJ, 282, 557

Hyman, J. 1979, in R. Vichnevetsky, R. S. Stepleman (eds.), Adv. in Comp. Meth. for PDE's—III, 313

Julien, K., Legg, S., McWilliams, J., Werne, J. 1996, Phys. Rev. E, 53, R5557

Julien, K., Werne, J. 1997, Phys. Lett. A, (submitted)

Keller, C. U., Von Der Luehe, O. 1992, A&A, 261, 321

Kerr, R. M. 1996, J. Fluid Mech., 310, 139

Kosovichev, A. G. 1996, ApJ, 461, L55

Lites, B. W., Nordlund, Å., Scharmer, G. S. 1989, in R. Rutten, G. Severino (eds.), Solar and Stellar Granulation, Vol. 263 of *NATO ASI C*, Kluwer Academic Press, 349

Malagoli, A., Cattaneo, F., Brummell, N. H. 1990, ApJ, 361, L33

Muller, R., Auffret, H., Roudier, T., Vigneau, J., Simon, G. W., Frank, Z., Shine, R. A., Title, A. M. 1992, Nat, 356, 322

Nesis, A., Bogdan, T. J., Cattaneo, F., Hanslmeier, A., Knoelker, M., Malagoli, A. 1992, ApJ, 399, L99

Nordlund, Å. 1975, A&A, 50, 23

Nordlund, Å. 1982, A&A, 107, 1

Nordlund, Å. 1985, Solar Physics, 100, 209

Nordlund, Å., Spruit, H. C., Ludwig, H.-G., Trampedach, R. 1997, A&A, (submitted)

Nordlund, Å., Stein, R. F. 1990, Computer Phys. Communications, 59, 119

Nordlund, Å., Stein, R. F. 1991a, in L. Crivellari, I. Hubeny, D. G. Hummer (eds.), Stellar Atmospheres: Beyond Classical Models, Kluwer

Nordlund, Å., Stein, R. F. 1991b, in D. Gough, J. Toomre (eds.), Challenges to Theories of the Structure of Moderate Mass Stars, Vol. 388 of *Lecture Notes in Physics*, Springer, Heidelberg, p. 141

Nordlund, A., Stein, R. F. 1996, in A. Noels, D. Fraipont-Cro, M. Gabriel, N. Grevesse, P. Demarque (eds.), Proceedings from the 32nd Liege Colloquium, Universite de Liege, Institut d'Astrophyique, p. 75

November, L. J., Simon, G. W. 1988, ApJ, 333, 427

Porter, D. H., Woodward, P. R. 1994, ApJS, 93, 309

Pulkkinen, P., Tuominen, I., A., B., Nordlund, Å., Stein, R. F. 1993, Astronomy and Astrophysics, 267, 265

Schrijver, C. J., Hagenaar, H. J., Title, A. M. 1997, ApJ, 475, 328

Solanki, S., Rüedi, I., Bianda, M., Steffen, M. 1996, A&A, 308, 623

Spruit, H. C. 1997, Mem. Soc. Astron. It.

Spruit, H. C., Nordlund, Å., Title, A. 1990, Annual Reviews of Astronomy and Astrophysics, 28, 263

Steffen, M., Ludwig, H.-G., Freytag, B. 1995, A&A, 300, 473

Stein, R. F., Nordlund, Å. 1989, ApJ, 342, L95

Stein, R. F., Nordlund, Å. 1991, in D. Gough, J. Toomre (eds.), Challenges to Theories of the Structure of Moderate Mass Stars, Vol. 388 of *Lecture Notes in Physics*, Springer, Heidelberg, p. 195

Stein, R. F., Nordlund, A. 1994, in D. Rabin, J. Jefferies, C. Lindsey (eds.), Infrared Solar Physics, IAU Symposium 154, Kluwer, Dordrecht, p. 225

Stein, R. F., Nordlund, Å., Kuhn, J. R. 1988, in E. J. Rolfe (ed.), Proc. Symp. Seismology of the Sun and Sun-like Stars, Vol. SP-286 of *ESA*, 529

Title, A. 1996, (private communication)

Title, A. M., Tarbell, T. D., Topka, K. P., Ferguson, S. H., Shine, R. A., SOUP Team, T. 1989, ApJ, 336, 475

Title, A. M., Topka, K. P., Tarbell, T. D., Schmidt, W., Balke, C., Scharmer, G. 1992, ApJ, 393, 782

Trampedach, R., Christensen-Dalsgaard, J., Nordlund, Å., Stein, R. F. 1997, in *Solar Convection, Oscillations and their Relationship*, eds. F.P.Pijpers, J. Christensen-Dalsgaard, C. Rosenthal, (Kluwer:Dordrecht) (in press)

Vincent, A., Meneguzzi, M. 1994, Jour. Fluid Mech., 258, 245

Vitense, E. 1953, Zs. f. Ap., 32, 135

Wang, Y., Noyes, R. W., Tarbell, T. D., Title, A. M. 1995, ApJ, 447, 419

Zocchi, G., Moses, E., Libchaber, A. 1990, Physica A, 166, 387

This 2-column preprint was prepared with the AAS LaTeX macros v4.0.